Published online 7 September 2017 *Nucleic Acids Research, 2017, Vol. 45, No. 19* **11425–11436**
doi: 10.1093/nar/gkx795

Activator Protein-1: redox switch controlling structure and DNA-binding

Zhou Yin[1], Mischa Machius[1], Eric J. Nestler[2] and Gabby Rudenko[1,*]

[1]Department of Pharmacology and Toxicology, and the Sealy Center for Structural Biology, University of Texas Medical Branch, Galveston, TX 77555, USA and [2]Fishberg Department of Neuroscience, Friedman Brain Institute, Icahn School of Medicine at Mount Sinai, 1 Gustave L Levy Place, New York, NY 10029, USA

Received July 09, 2017; Revised August 24, 2017; Editorial Decision August 28, 2017; Accepted August 31, 2017

ABSTRACT

The transcription factor, activator protein-1 (AP-1), binds to cognate DNA under redox control; yet, the underlying mechanism has remained enigmatic. A series of crystal structures of the AP-1 FosB/JunD bZIP domains reveal ordered DNA-binding regions in both FosB and JunD even in absence DNA. However, while JunD is competent to bind DNA, the FosB bZIP domain must undergo a large conformational rearrangement that is controlled by a 'redox switch' centered on an inter-molecular disulfide bond. Solution studies confirm that FosB/JunD cannot undergo structural transition and bind DNA when the redox-switch is in the 'OFF' state, and show that the mid-point redox potential of the redox switch affords it sensitivity to cellular redox homeostasis. The molecular and structural studies presented here thus reveal the mechanism underlying redox-regulation of AP-1 Fos/Jun transcription factors and provide structural insight for therapeutic interventions targeting AP-1 proteins.

INTRODUCTION

Many transcription factors are under redox regulation, including the activator protein-1 (AP-1), one of the earliest identified (1–4). AP-1 is a heterodimer composed of Fos, Jun, ATF and Maf proteins; it binds to cognate DNA (an 'AP-1 site') and regulates gene expression, controlling cellular events such as differentiation, proliferation and apoptosis (5). The prototype AP-1 c-Fos/c-Jun bZIP domain contains two inter-coiled helices held together by a leucine zipper that forms a forceps-like structure and two helical basic regions that insert into the major grooves of DNA (Figure 1A) (6). Conserved leucines at d-positions of helical heptad repeat 1 through 5 assemble the coiled-coil architecture of the leucine zipper in the dimer, and a consensus motif (NxxAAxxCR) from each monomer interacts with the palindromic AP-1 site (TGA(G/C)TCA) (6,7) (Figure 1A). Related bZIP protein families, e.g. CREB, NFE2 and BACH, share these conserved residues (3) (Figure 1A; Supplementary Figure S1).

Binding of AP-1 to DNA is controlled by redox regulation, but the underlying mechanism has remained enigmatic (1,4,8), perhaps because in the absence of DNA, the binding region has been presumed to be unfolded in AP-1 (9,10) and other bZIP transcription factors in general (11). To address this gap, we solved a series of crystal structures of the human FosB/JunD bZIP heterodimer (hitherto referred to as FosB/JunD), an AP-1 complex prominent in brain (12). By comparing our crystal structures of FosB/JunD in presence and absence of DNA, we reveal that, while both FosB and JunD contain ordered DNA-binding modules even in absence of DNA, at least in the crystalline state, only JunD is in a conformation to bind DNA. The FosB bZIP domain must undergo a large conformational rearrangement in order to bind DNA, which is controlled by a 'redox switch' centered on an inter-molecular disulfide bond between FosB and JunD. Together with solution-based studies, our data reveal the structural basis for redox control of AP-1 transcription factors such as FosB/JunD.

MATERIALS AND METHODS

Oligonucleotides

The sense and antisense strands of a 19-mer oligo DNA (5′-CGTCGGTGACTCAAAACAC-3′; AP-1 site underscored) derived from the AP-1 site in the cyclin-dependent kinase 5 promoter labelled with TAMRA at both 5′-ends were purchased from Sigma Aldrich. The sense and antisense strands of an oligo DNA 5′-(CGTCGGTGACTCACCGACG-3′; AP-1 site underscored) engineered to be fully palindromic to promote crystallization were purchased from Sigma Aldrich. Oligo DNA was annealed by mixing equivalent molar quantities of the complementary strands and heating them to 95°C for 2.5 min, followed by slow cooling to room temperature (∼1 min/°C). Annealed oligo DNA were checked for purity by electrophoresis on polyacrylamide gels stained with ethidium bromide.

*To whom correspondence should be addressed. Tel: +1 409 772 6292; Fax: +1 409 772 9642; Email: garudenk@utmb.edu

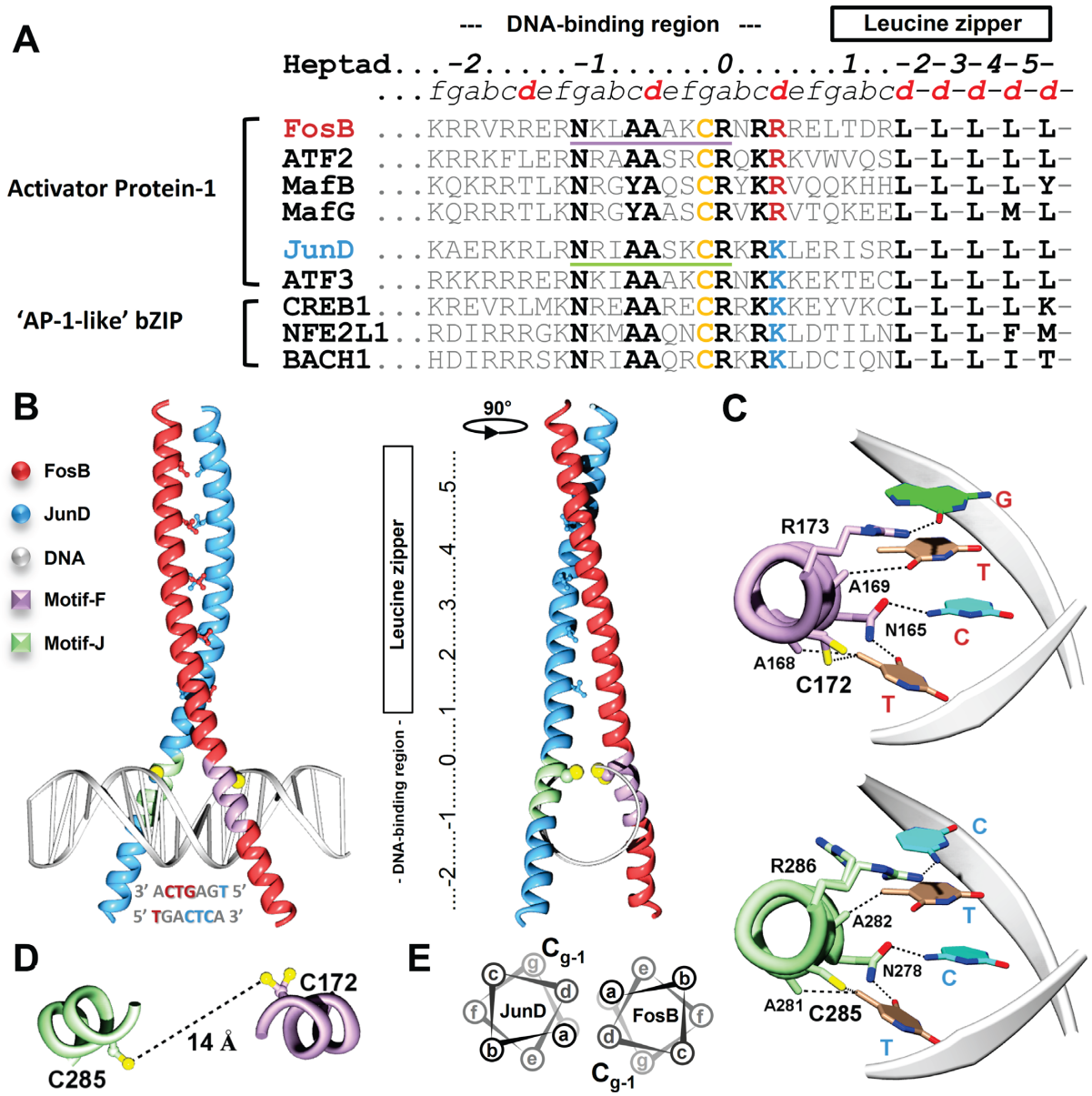

Figure 1. FosB/JunD bound to cognate DNA. (**A**) bZIP domain with leucine zipper and DNA binding regions (top). Only the d-position residues are displayed for Heptad 2–5 for simplicity. Consensus motif NxxAAxxCR in human AP-1 and 'AP-1-like' bZIP domains binds DNA (bottom). For emphasis, FosB C^{172} and its counterparts are highlighted in golden, while FosB R^{176} and its counterparts are highlighted red (Arg) or blue (Lys) respectively. (**B**) FosB/JunD bound to an AP-1 site (FJ-DNA type I), front and side view. Leucines at the d-positions are shown. C^{172} (FosB) and C^{285} (JunD) are depicted as yellow spheres. (**C**) Consensus motif (NxxAAxxCR) of FosB (Motif-F, N^{165}-R^{173}; top) and JunD (Motif-J, N^{278}-R^{286}; bottom) bound to palindromic AP-1 DNA. Bases in contact with protein residues are colored (G: green; T: brown and C: cyan). The closest key contacts (< 5Å) between side chains and bases are shown as dashed lines. C^{172} (FosB) occupies alternate conformations. (**D**) Distance between the thiol groups of C^{172} (FosB, conformer A) and C^{285} (JunD). (**E**) Helical wheel indicating the locations of C^{172} (FosB) and C^{285} (JunD). Color scheme for (B–D) is displayed at the upper-left corner of B (FosB: red; JunD: blue; DNA: grey; Motif-F: lilac; Motif-J: light green). Non-carbon atoms in red (oxygen), blue (nitrogen), and yellow (sulfur).

Molecular cloning

The *Homo sapiens* FosB bZIP domain (residues E^{153}-K^{219}) was sub-cloned into a pET21-NESG expression vector using the cDNA of *Mus musculus* FosB gene as a template because the sequences are identical. The *H. sapiens* JunD bZIP domain (residues Q^{266}-V^{332}) was cloned into a pET21a expression vector (Genscript). Each of the constructs has an N-terminal hexa-histidine tag followed by a tobacco etch virus (TEV) protease cleavage site. Plasmids verified by DNA sequencing were transformed into chemically competent *Escherichia coli* Rosetta 2 (DE3) cells (Invitrogen).

Protein production and purification

To express recombinant proteins, a culture of *E. coli* strain Rosetta 2 (DE3) grown in LB media at 37°C to a density of 0.6 (595 nm) was induced overnight with 0.5 mM isopropyl β-D-thiogalactoside (IPTG) at 16°C. The harvested cells were re-suspended in lysis buffer (20 mM Tris–HCl,

pH 8, 1 M NaCl, 0.5 M NaBr, 20 mM imidazole and 2 mM Tris(2-carboxyethyl)phosphine (TCEP)), lysed by sonication, and centrifuged at 18 000 rpm (46 285 g) for 30 min. The supernatant was loaded onto a Ni-NTA agarose column (Invitrogen), washed with lysis buffer, and eluted in the same buffer containing 0.5 M imidazole. The eluted protein was then cleaved with His-tagged TEV protease to remove the histidine tag while dialyzing against 20 mM Tris–HCl, pH 8, 1 M NaCl and 2 mM TCEP overnight to remove the imidazole. Cleaved and dialyzed protein was then again loaded onto the Ni-NTA agarose column, and the flow-through containing the histidine tag-free protein was collected.

In vitro reconstitution, air-oxidation and size-exclusion chromatography

FosB and JunD bZIP domains individually produced were mixed at equal molar, and subjected to size-exclusion chromatography using a HiLoad 16/600 Superdex 200 pg column (GE Healthcare) equilibrated with 20 mM HEPES, pH 7, 0.5 M NaCl and 1 mM DTT. Peak fractions containing the reduced FosB/JunD (FJ^{red}) heterodimer (as detected by SDS-PAGE) were pooled, concentrated and reapplied 5–10 times to improve homogeneity. The oxidized form of FosB/JunD (FJ^{oxi}) was generated by dialyzing purified FJ^{red} overnight against 20 mM HEPES, pH 7 and 0.5 M NaCl to remove reducing agent while exposing to ambient air. After completion of the conversion of FJ^{red} to FJ^{oxi} (as assessed by non-reducing SDS-PAGE), FJ^{oxi} was reloaded on a size-exclusion column in the same buffer to ensure homogeneity. DNA-bound, reduced FosB/JunD was generated by mixing purified FJ^{red} with oligo-DNA containing the AP-1 site at equal molar and purification with size-exclusion chromatography in a buffer containing 20 mM Tris–HCl, pH 8, 50 mM NaCl and 1 mM TCEP. Finally, all proteins and protein–DNA complexes were concentrated to 10–20 mg/ml, aliquoted and flash frozen. The final protein purity was analyzed by SDS-PAGE (purity > 95%).

Crystallization and X-ray data collection

Two crystal forms were grown for FosB/JunD in complex with DNA. FJ-DNA Type I crystals were grown at 293 K with the hanging-drop vapor-diffusion method by mixing 0.5–1 μl of FosB/JunD-DNA complex (8 mg/ml protein in 20 mM Tris–HCl, pH 8, 50 mM NaCl, 1 mM TCEP) with an equal volume of reservoir solution consisting of 0.9 M Na_2HPO_4 and 24% (v/v) ethylene glycol. FJ-DNA Type II crystals were obtained similarly but without ethylene glycol in the reservoir. Serial streak seeding was performed to improve crystal morphology. FJ-DNA Type I crystals were transferred to reservoir solution and then cryo-cooled by plunging into liquid nitrogen; FJ-DNA Type II crystals were cryo-protected by adding 20% (v/v) ethylene glycol to the reservoir solution before cryo-cooling. Diffraction data on Type I and II FJ-DNA crystals were collected at 100 K at the Advanced Photon Source (APS), Argonne National Laboratory (ANL), Argonne, IL beamline 19-ID using X-rays of wavelength 0.979 Å. Four different crystal forms of FosB/JunD in the DNA-free form were obtained. FJ crystals were grown at 293 K with the sitting-drop vapor-diffusion method by mixing 0.5–1 μl of FosB/JunD (10 mg/ml protein dialyzed against 20 mM HEPES, pH 7, 50 mM NaCl and 1 mM TCEP) with an equal volume of reservoir solution consisting of 3 M 1,6-hexanediol, 50 mM Tris, pH 8.5 and 5 mM $MgCl_2$. Crystals were cryo-protected by transferring them to reservoir solution and then cryo-cooled by plunging them into in liquid nitrogen. Diffraction data were collected on a single FJ crystal at 100 K at the APS Beamline 17-ID using X-rays of wavelength 0.9999 Å. FJ^{oxi} Type I crystals were grown at 293 K with the sitting-drop vapor diffusion method by mixing 0.5 μl of FJ^{oxi} (20 mg/ml protein in 20 mM HEPES, pH 7, and 50 mM NaCl) with 0.5 μl of reservoir solution consisting of 45% (v/v) 2-methyl-2,4-pentanediol (MPD), 0.3 M NaCl and 0.1 M HEPES, pH 7.5. Serial streak seeding was performed to improve crystal morphology. Crystals were cryo-cooled directly from the mother liquor by plunging into liquid nitrogen. FJ^{oxi} Type II crystals were grown at 293 K with the hanging-drop vapor diffusion method by mixing 0.3–1 μl of FJ^{oxi} (20 mg/ml protein in 20 mM HEPES, pH 7, 50 mM NaCl) with 1 μl of reservoir solution consisting of 12% (v/v) ethanol, 0.3 M NaCl and 2% (v/v) Jeffamine M-600. Crystals were cryo-protected in reservoir solution containing 20% (v/v) ethylene glycol and flash-cooled by plunging into liquid nitrogen. FJ^{oxi} Type III crystals were grown at 293 K with the hanging-drop vapor diffusion method by mixing 1 μl of FosB/JunD (8.5 mg/ml protein dialyzed into 20 mM sodium cacodylate, pH 7, 50 mM NaCl and 3 mM DTT) with 1 μl of reservoir solution consisting of 20% (v/v) MPD, 0.1 M NaCl, 50 mM sodium cacodylate, pH 6, and 10 mM spermine. Crystals were cryo-cooled directly from the mother liquor by plunging into liquid nitrogen. Diffraction data were collected on a single FJ^{oxi} crystal of type I, II or III at 100 K at the APS beamline 21-ID-F using X-rays of wavelength 0.9787 Å.

Data processing, structure solution and refinement

Diffraction data sets were collected from single crystals. Data were processed, and the integrated intensities merged and reduced in HKL2000 (13) by using automatic correction procedures. The resolution cut-off was generally set to $I/\sigma(I) = 2$ (as defined by HKL2000). The FJ-DNA (Type I and II) crystal structures were solved by molecular replacement with the program PHASER (14) in PHENIX (15) using the human c-FOS/c-JUN:DNA complex (Protein Data Bank entry 1FOS (6)) as the search model. FJ and FJ^{oxi} structures were solved by molecular replacement using the Leucine Zipper of the FJ-DNA Type I structure as the search model. Iterative cycles of model building and refinement were carried out with COOT (16) and PHENIX.refine (17) using riding hydrogen atoms added to all models, translation-libration-screw rotation (TLS) parameterization by TLSMD analysis (18) and validation with MolProbity (19). Ramachandran plot statistics (favoured/allowed/disallowed) of the final models are: FJ-DNA type I (99.6/0.4/0), FJ-DNA type II (99.2/0.8/0), FJ (98.1/1.9/0), FJ^{oxi} type I (100.0/0/0), FJ^{oxi} type II (98.7/1.3/0) and FJ^{oxi} type III (98.3/1.7/0). For detailed statistics for data collection and refinement see Table 1. Coordinates and structure factors of FJ-DNA (Type I and II),

FJ and FJ^{oxi} Type I, II and III) can be accessed *via* Protein Data Bank IDs: 5VPE, 5VPF, 5VPA, 5VPB, 5VPC and 5VPD respectively.

Molecular graphics

Molecular graphics representations were created using the software CCP4mg v2.9.0 (20). Molecular graphical movies were produced using the UCSF Chimera package (21). Figure 1B–D: Chain A/B (FosB/JunD) and E/F (AP-1 DNA) of FJ-DNA type I crystal structure are displayed. Figure 2A: Chain C/D (FosB/JunD) of FJ^{oxi} type I crystal structure are displayed. Figure 2B and C: Chain C/D (FosB/JunD) of FJ^{oxi} type I crystal structure and Chain A/B (FosB/JunD) of FJ crystal structure are displayed. Figure 3: Chain C/D (FosB/JunD) of FJ^{oxi} type I crystal structure and Chain A/B (FosB/JunD) and E/F (AP-1 DNA) of FJ-DNA type I crystal structure are displayed. Chain D (FJ^{oxi}) and Chain B (FJ-DNA) are superimposed and shown in the main figure. Residues range (N^{278}-R^{286}) of both chains are superimposed and shown in the inset figures. Figure 4A: Chain C (FosB) and D (JunD) of FJ^{oxi} type I crystal structure and Chain A (FosB) and B (JunD) of FJ-DNA type I crystal structure are displayed. Figure 4B: Inset: Chain C/D (FosB/JunD) of FJ^{oxi} type I crystal structure are displayed. Figure 5A-D: Chain C/D (FosB/JunD) of FJ^{oxi} type I crystal structure and Chain A/B (FosB/JunD) and E/F (AP-1 DNA) of of FJ-DNA type I crystal structure are displayed. Overall view: JunD residue range N^{278}-S^{330} of Chain D (FJ^{oxi} type I) and Chain B (FJ-DNA) are superimposed. K_{d0} attack: JunD residue range N^{278}-R^{285} of Chain D (FJ^{oxi} type I) and Chain B (FJ-DNA) are superimposed. Kink-helix transition: FosB residue range E^{178}-R^{182} of Chain C (FJ^{oxi} type I) and Chain A (FJ-DNA) are superimposed. Site-recognition: FosB residue range N^{165}-R^{173} of Chain C (FJ^{oxi} type I) and Chain A (FJ-DNA) are superimposed. Figure 6: FJ and FJ^{oxi} (type I) crystal structures are displayed. Movie S1: Chain C/D (FosB/JunD) of FJ^{oxi} type I crystal structure, Chain A/B (FosB/JunD) of FJ crystal structure and Chain A/B (FosB/JunD) and E/F (AP-1 DNA) of FJ-DNA type I crystal structure are shown. Movie S2: Chain A/B/C/D (FosB/JunD dimer-of-dimers) of FJ^{oxi} type I crystal structure is shown.

Bioinformatics

Sequence alignment of human bZIP transcription factors (NCBI IDs: FosB: NP_006723.2; c-Fos: NP_005243.1; Fra1: NP_005429.1; Fra2: NP_005244.1; JunD: NP_005345.3; c-Jun: AAH68522.1; JunB: AAA74915.1; ATF2: NP_001243022.1; ATF7: NP_006847.1; CREBpa: AAC37527.1; MafA: NP_963883.2; MafB: NP_005452.2; c-Maf: AAC27038.1; NRL: NP_006168.1; MafK: NP_002351.1; MafF: NP_001155045.1; MafG: NP_116100.2; ATF3: NP_001025458.1; JDP2: NP_001128520.1; CREB1: NP_604391.1; CREM: AAC60616.2; ATF1: NP_005162.1; NF-E2 p45: NP_001248390.1; NF-E2 L1: AAH10623.1; NF-E2 L2: NP_006155.2; NF-E2 L3: NP_004280.5; BACH1: BAA24932.1; BACH2: NP_001164265.1) was carried out using COBALT (22).

Mass spectrometry

Matrix-Assisted Laser Desorption Ionization Time-of-Flight Mass Spectrometry (MALDI TOF/TOF MS, Sciex 5800) was used to analyze protein molecular weights. Protein samples (1 μL) were spotted on a 384 Opti-TOF 123 mm × 81 mm SS plate, dried, sinapinic acid solution (1 μL) added and dried again. Cytochrome *c* solution was spotted next to samples for external calibration. The instrument was operated in positive ion linear mode with mass range 3–12 kD. A fixed laser intensity of 6 K was used, and a total of 5000 samples were taken. Intensity data were normalized with the highest peak set at 100%. Figures were made with GraphPad Prism v5.01 (GraphPad Software).

Determination of midpoint redox potential

FJ^{oxi} samples serially diluted in the absence and presence of 5 mM DTT were resolved with non-reducing SDS-PAGE on 15% gels, stained with silver nitrate, and quantified with ImageJ software (National Institutes of Health) to determine the densitometric linear range of the protein concentration. The redox potential of FosB/JunD was determined following a previously published procedure (23). FJ^{oxi} (50 nM, Mw heterodimer) was added to aliquots of buffer containing 20 mM HEPES at pH 7, 50 mM NaCl and 200 mM trans-4,5-dihydroxy-1,2-dithiane (the oxidized form of DTT, DTT^{ox}). DTT was then added to the aliquots in a two-fold serial dilution from 5 mM to 10 μM to establish a gradient of half-cell redox potential (E_h). The E_h of each aliquot containing the DTT/DTT^{ox} redox couple was determined according to the Nernst equation for a two-electron redox reaction: $E_h = E_0 + 2.3 \times RT/nF \times \log([DTT^{ox}]/[DTT])$, where $E_0 = -330$ mV at pH 7, and $n = 2$ (24). Control experiments were carried out without DTT^{ox} in the reaction system to ensure the reduction capacity of DTT. Samples were equilibrated at room temperature for 2 h before the reaction was quenched with 5 × non-reducing SDS-loading buffer containing 200 mM *n*-ethylmaleimide (NEM). The oxidized/reduced forms of FosB/JunD (FJ^{oxi} and FJ^{red}) were resolved with non-reducing SDS-PAGE on a 15% gel stained with silver nitrate and quantified by densitometry. In order to determine the fraction of FJ^{oxi} and FJ^{red} in each aliquot, densitometric data of FJ^{oxi} and FJ^{red} were normalized to correct for differences in staining efficiency between the FJ^{oxi} (a single band) and FJ^{red} (the FosB and JunD bands combined). As an internal control on each gel, the ratio of band density of FJ^{oxi} (with minimal DTT) /FJ^{red} (with maximal DTT) was used as a correction factor; the band intensity of FJ^{red} in each aliquot was then multiplied by this correction factor. The band intensity of FJ^{oxi} and corrected band intensity of FJ^{red} was used to calculate the fraction of FJ^{oxi} and FJ^{red} ($[FJ^{oxi}]/[FJ^{red}]$) that was fitted to the two-electron Nernst equation, $E_h = E_m + 2.3 \times RT/nF \times \log([FJ^{oxi}]/[FJ^{red}])$, where $n = 2$. The midpoint redox potential (E_m) at pH 7 was determined by iterative curve fitting using GraphPad Prism v5.01 (GraphPad Software). All E_m values reported correspond to the average of three independent titrations.

Table 1. Data collection and refinement statistics for the FosB/JunD and FosB/JunD+DNA crystal structures

	FJ-DNA, Type-I	FJ-DNA, Type-II	FJ	FJ^{oxi}, Type-I	FJ^{oxi}, Type-II	FJ^{oxi}, Type-III
Crystallization conditions	0.9 M Na_2HPO_4 and 24% (v/v) ethylene glycol	0.9 M Na_2HPO_4	3 M 1,6-Hexanediol, 50 mM Tris pH 8.5 and 5 mM $MgCl_2$	45% (v/v) 2-methyl-2,4-pentanediol (MPD), 0.3 M NaCl and 0.1 M HEPES pH 7.5	12% (v/v) ethanol, 0.3 M NaCl and 2% (v/v) Jeffamine M-600	20% (v/v) 2-methyl-2,4-pentanediol (MPD), 0.1 M NaCl, 50 mM sodium cacodylate pH 6 and 10 mM spermine
Data collection						
Wavelength (Å)	0.979 Å	0.979 Å	0.9999 Å	0.9787 Å	0.9787 Å	0.9787 Å
Space group	*C*2	$P6_122$	*I*222	*C*2	*C*2	$P2_12_12$
Cell dimensions						
a, *b*, *c* (Å)	116.48, 90.76,105.62	119.64, 119.64, 249.97	52.61, 95.35, 98.20	92.83, 99.26, 49.86	111.18, 49.95, 97.75	92.01, 98.05, 50.25
α, β, γ (°)	90, 117.93, 90	90, 90, 120	90, 90, 90	90, 109.40, 90	90, 122.94, 90	90, 90, 90
Resolution (Å)	47.31–2.05 (2.10–2.05)	48.59–2.69 (2.75–2.69)	34.20–2.83 (2.85–2.83)	43.74–2.69 (2.75–2.69)	44.04–2.50 (2.54–2.50)	44.72 -2.79 (2.82–2.79)
Unique reflections	58932 (2933)	30141 (1469)	6010 (301)	11872 (595)	15500 (743)	11778 (571)
R_{merge}	0.055 (0.931)	0.107 (1.752)	0.096 (1.167)	0.064 (0.641)	0.071 (0.582)	0.108 (0.906)
R_{pim}	0.024 (0.414)	0.029 (0.462)	0.033 (0.390)	0.038 (0.384)	0.043 (0.349)	0.043 (0.363)
$I/\sigma(I)$	27.6 (2.0)	27.1 (2.0)	25.0 (2.2)	20.0 (2.0)	17.0 (2.2)	27.6 (2.0)
Completeness (%)	98.3 (98.2)	99.9 (100.0)	100.0 (100.0)	99.9 (100)	99.7 (100.0)	99.9 (100)
Multiplicity	6.1 (5.9)	15.7 (15.5)	9.5 (9.5)	3.8 (3.8)	3.8 (3.8)	7.1 (7.1)
Refinement[b]						
Resolution (Å)	47.31–2.05 (2.10–2.05)	48.59–2.69 (2.76–2.69)	34.20–2.83 (3.24–2.83)	43.74–2.69 (2.83–2.69)	44.04–2.50 (2.59–2.50)	44.72 -2.79 (2.92–2.79)
R_{work}/R_{free}	0.218/0.254 (0.300/0.386)	0.210/0.248 (0.276/0.326)	0.245/0.283 (0.272/0.337)	0.238/0.275 (0.319/0.444)	0.251/0.289 (0.302/0.347)	0.249/0.300 (0.326/0.356)
Total No. of Reflections	53064 (1761)	27337 (1360)	4417 (775)	10200 (719)	14088 (606)	10786 (772)
Reflections used for R_{free}	2000 (66)	1999 (99)	433 (76)	1021 (72)	1401 (63)	1068 (70)
Non-hydrogen atoms	4047	3928	906	1940	1943	1996
Protein	2284	2189	899	1916	1907	1987
DNA	1470	1523	N/A	N/A	N/A	N/A
Ligands/ions	63	45	2	13	6	5
Water	230	71	5	11	30	4
B factors (Å^2), overall	36.7	46.2	58.4	48.9	57.4	49.1
Protein	36.0	44.6	58.7	48.9	57.7	49.1
DNA	40.0	48.9	N/A	N/A	N/A	N/A
Ligands/ions	74.0	61.7	46.8	60.2	58.4	61.6
Water	33.6	29.3	14.7	24.9	37.1	20.6
r.m.s. deviations						
Bond lengths (Å)	0.005	0.006	0.006	0.002	0.003	0.003
Bond angles (°)	0.75	0.79	0.69	0.42	0.51	0.59
Ramachandran plot (%)						
favored	99.6	99.2	98.1	100.0	98.7	98.3
allowed	0.4	0.8	1.9	0	1.3	1.7
disallowed	0	0	0	0	0	0
Rotamer Outliers, *n* (%)	2 (0.8)	0 (0)	1 (1.1)	1 (0.5)	1 (0.5)	1 (0.5)

[a]Numbers in parentheses refer to the highest-resolution shell. r.m.s., root-mean-square.
[b]Hydrogen atoms were added to the riding positions of all models in refinements.

Circular dichroism spectroscopy

Circular dichroism measurements were performed on a J-815 Spectropolarimeter (JASCO) equipped with Peltier junction temperature controller at 20 °C using a quartz cuvette with 1 mm path length. Spectra were recorded at 0.5 nm intervals from 190 to 250 nm with a 1 nm bandwidth. Spectra were averaged over three scans, buffer spectra subtracted and then converted to mean residue ellipticity ([θ]). Protein concentrations were determined by measuring the UV absorbance at 215 nm with a DeNovix DS-11+ spectrophotometer using a percent extinction coefficient ($E = 0.1\%$) of 11.7 for a 1 mg/ml (0.1%) solution of peptide as defined by the manufacturer. Ellipticity of FJ^{oxi} at 0.1 mg/ml (6 μM as heterodimer) in a buffer of 12.5 mM K_2HPO_4/KH_2PO_4, pH 7.0, and 50 mM NaF were measured in the absence and presence of 7 μM cognate DNA, with or without 1 mM TCEP. Ellipticity of 7 μM cognate DNA was measured in the same buffer for comparison. Helical content (% helicity) is calculated as $100 \times ([\theta]_{222nm} / {}^{max}[\theta]_{222nm})$; $[\theta]_{222nm}$ is [θ] measured at 222 nm and ${}^{max}[\theta]_{222nm}$ is maximal [θ] at 222 nm estimated as $-40\,000 \times [1 - (2.5/n)]$, where $n = 67$, the number of residues in a monomer helix of FosB or JunD (25). Figures were made using Excel 2013 (Microsoft Corporation) and GraphPad Prism v5.01 (GraphPad Software).

Protein labelling

To label FJ^{oxi} using amide coupling, a sample (2 mg/ml, 120 μM, M_w heterodimer) was incubated with 1 mM (5/6) TAMRA-SE (G-Biosciences) in 20 mM HEPES, pH 7.0, 50 mM NaCl at room temperature for 10 min. Labeled protein was separated from unreacted fluorophore by two passes over a SpinOUT GT-600 desalting column (G-Biosciences). The protein concentration of TAMRA-labelled protein was determined using UV absorption at 247 nm, where TAMRA has an extinction coefficient of 80 000 cm^{-1} M^{-1}. A labelling efficiency of 1.05 mol of TAMRA per mol of FJ^{oxi} was obtained.

Fluorescence-based equilibrium titration

Titration experiments were conducted in non-treated black 96-well plates (Corning) using a PHERAstar microplate reader (BMG Labtech) with the fluorescence polarization module for TAMRA (Excitation/emission wavelength at 540 nm/590 nm). For each experiment, the gain of the parallel and perpendicular channel was calibrated with

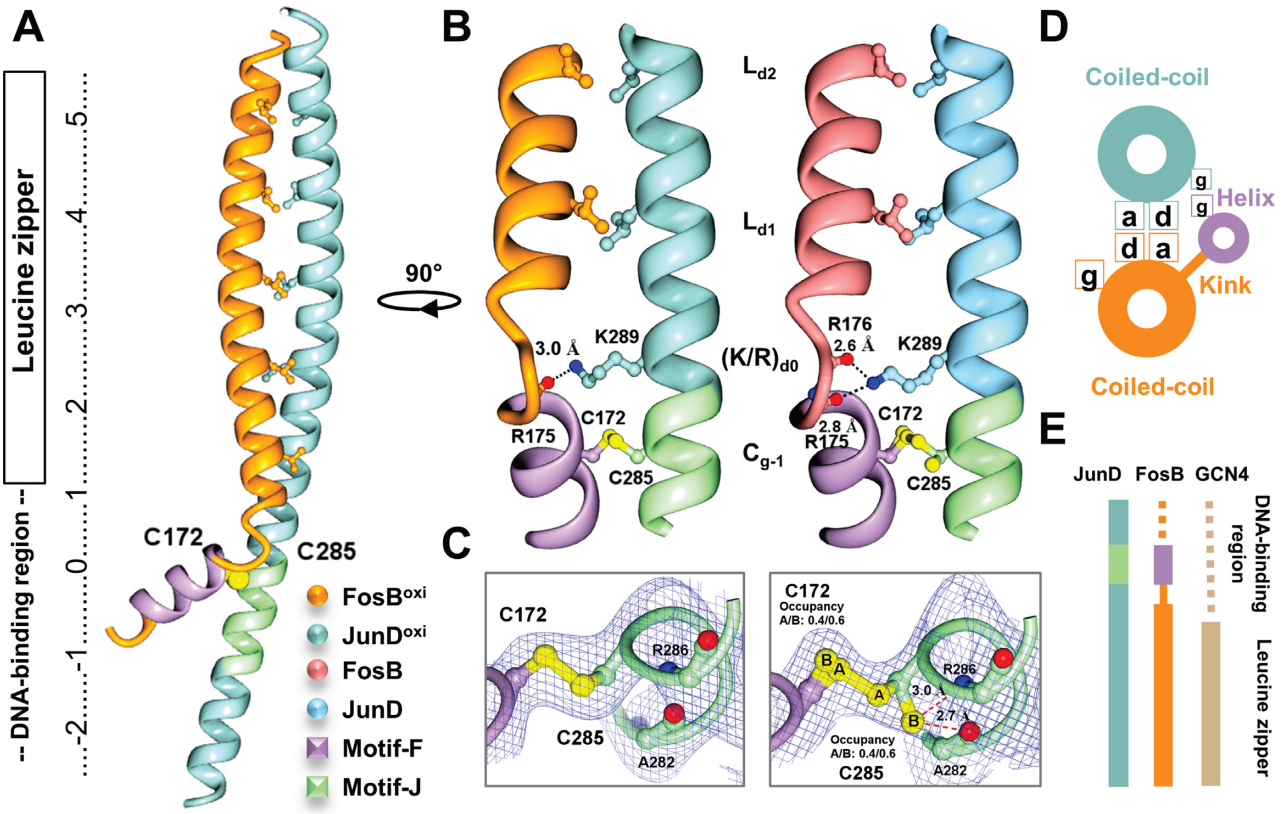

Figure 2. FosB/JunD in the DNA-free form. (**A**) FosB/JunD dimer in FJ^{oxi} (type I). Leucines at the d-positions are shown. (**B**) Dimer interface of FJ^{oxi} type I (left) and FJ crystal (right) structures showing Heptad -1 to Heptad 2. Key hydrogen bonds in dashed lines. (**C**) Composite omit electron density map around the FosB/JunD C^{172}/C^{285} disulfide bond (contoured at 1.0 σ) in the fully oxidized FJ^{oxi} type I (left) and partially oxidized FJ (right) heterodimer. Relevant side chains (C^{172}, C^{285}), backbone atoms (R^{286}, A^{282}) and distances, as discussed in the text. (**D**) Adapted helical wheel of the interface between FosB (orange, purple)/JunD (cyan) depicting the a/d/g-residues of the heptad repeat preceding and following the kink in FosB. (**E**) Schematic representation of FosB, JunD and GCN4 monomers in the DNA-free form. Bars represent helices; thin bars, kinks; dots, disordered peptide. Color scheme is indicated in (A) and applies to all sub-figures. Non-carbon atoms are colored as in Figure 1.

TAMRA in water so it has a polarization value of 50 mP and a fluorescence intensity close to that of the labelled protein or DNA. A blank control (buffer only) was subtracted from intensity readings for all experiments. Titration of FosB/JunD oligomerization was carried out by serial dilution of 50 μM FJ^{oxi} (M_w heterodimer) with buffer (20 mM HEPES, pH 7.0, 50 mM NaCl) added with 0.1 μM TAMRA-labelled FJ^{oxi} (M_w heterodimer) as a tracer. Titration of the saturation binding of FosB/JunD to DNA was carried out by serial dilution of 600 nM FJ^{oxi} with buffer (20 mM Tris–HCl, pH 8.0, 50 mM NaCl, 0.02% Nonidet P-40) added with 10 nM TAMRA-labeled DNA as a tracer. For experiments with reduced protein, TCEP was added to a final concentration of 1 mM. All titrations were carried out in duplicates. Fluorescence intensity and polarization data were computed with the MARS Data Analysis Software v3.01 (BMG Labtech). Intensity readings (F) were normalized (F/F_0) (whereby F_0 is the intensity at zero concentration of titrant). Curves of FosB/JunD oligomerization were fit using GraphPad Prism v5.01 (GraphPad Software). Curves for FosB/JunD oligomerization were fit to a mathematical model of dimer–tetramer equilibrium adapted from published methods (26). The binding–saturation curves were fit to a mathematical model of one-site specific binding with ligand depletion (27).

Analytical ultracentrifugation

Sedimentation velocity experiments were performed at 20°C in a Beckman Coulter Model XL-A analytical ultracentrifuge using double-sector quartz cells and an An-60 Ti rotor. FJ^{oxi} at three concentrations (M_w heterodimer): 3 μM (in 12.5 mM K_2HPO_4/KH_2PO_4, pH 7.0, 50 mM NaF), 30 or 300 μM (both in 20 mM HEPES, pH 7.0, 50 mM NaCl) in a sample volume of 350–400 μl were loaded into the sample cells. Buffer in a volume of 420 μl was loaded into the reference cells. For experiments with reduced protein, 1 mM TCEP was added to both buffer and sample. The optimal wavelengths to measure the absorbance of the samples were determined with test scans carried out at 3000 rpm. Production scans of absorbance at 202, 230 or 242 nm were carried out, one per 10 min, at 50 000 rpm (201 240 g) with a step size of 0.003 cm. Solvent density, solvent viscosity, and estimates of the partial specific volume of FosB/JunD bZIP heterodimer (0.737 ml/g) at 20°C were calculated using SEDNTERP (28). Data were fitted to a continuous size-distribution model using SEDFIT software (29–31). Fig-

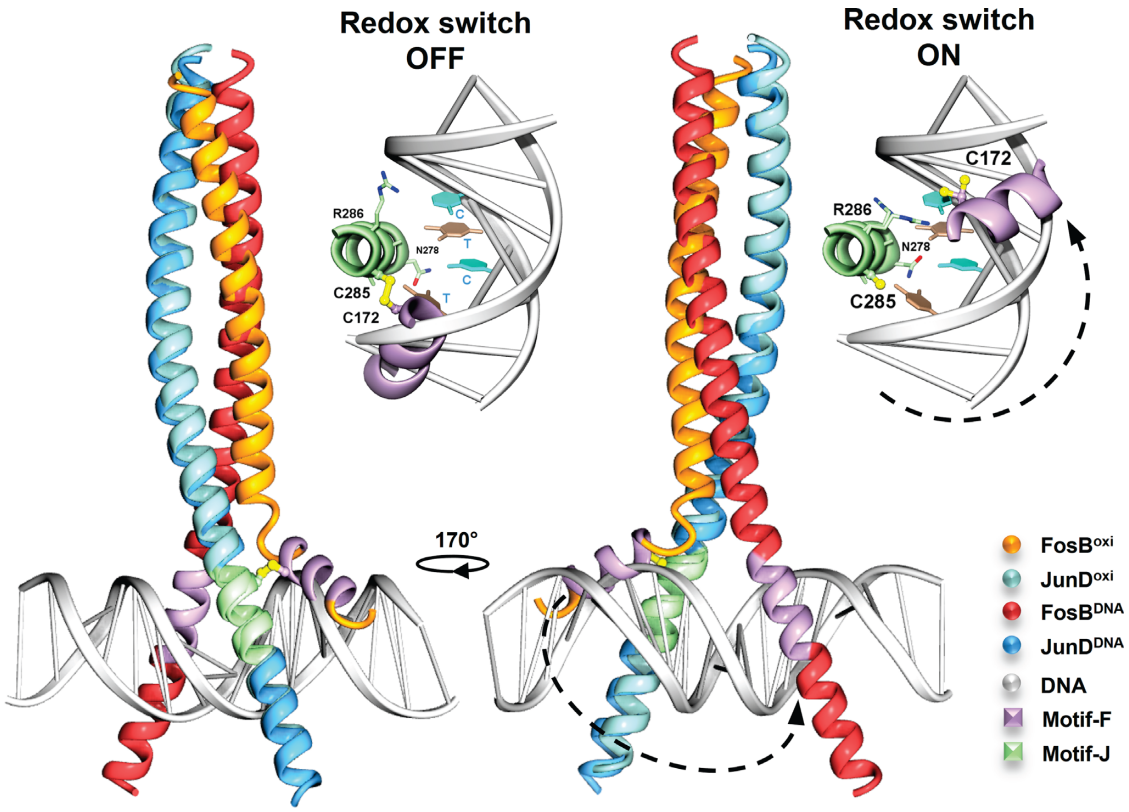

Figure 3. Structural mechanism of the redox regulation of FosB/JunD through coupled DNA-binding and structure transition. FJ^{oxi} (type I) is superimposed onto FJ-DNA (type I) by matching the JunD molecules, respectively. Two views separated by 170° are shown. Insets show a zoomed-in view of the DNA-binding consensus motifs of JunD (Motif-J) and FosB (Motif-F), depicting the redox switch 'OFF' and 'ON' states. Dashed lines indicate conformational changes. Color scheme is indicated in the key.

ures were made using Excel 2013 (Microsoft Corporation) and GraphPad Prism v5.01 (GraphPad Software).

RESULTS AND DISCUSSION

Crystal structures of FosB/JunD bound to AP-1 DNA

We first determined the structure of FosB/JunD bound to an AP-1 site in two forms at 2.1 and 2.7 Å resolution, respectively (FJ-DNA type I and II) (Figure 1B; Supplementary Figure S2A; crystallographic data shown in Table 1). Both structures show a canonical 'Y-shaped' bZIP-DNA complex with residues K^{157}-R^{176} (FosB) and K^{270}-K^{289} (JunD) interacting with DNA. The consensus motifs NxxAAxxCR of FosB/JunD interact exclusively with the nucleic acid bases of the AP-1 site, and extend the helices forming the leucine zipper (Figure 1C). Though FosB and JunD both contain this motif, in FosB, the conserved R^{173} (R_{a0}, based on its position in the heptad repeats) interacts with the central G of the AP-1 DNA palindrome, while in JunD, the corresponding R^{286} (R_{a0}) interacts with the central C; thus the DNA binds only in one orientation in our crystal structures (Supplementary Figure S2B). A preferred orientation of DNA binding is consistent with prior electrophoresis-based studies (32), but not with the crystal structure of c-Fos/c-Jun+DNA where no preference was seen, possibly because C^{154} (c-Fos) and C^{272} (c-Jun) at the C_{g-1} position in the DNA-binding consensus motif were mutated to serine (6).

It has been proposed that in the AP-1 c-Fos/c-Jun heterodimer the cysteines in the DNA-binding motif (C_{g-1}) are under redox-control and decrease DNA binding upon oxidation, for example, by forming an intermolecular disulfide bond (4,8). In our FosB/JunD+DNA structures, C^{172} (FosB) and C^{285} (JunD) are located 14 Å apart (Figure 1B and D). Furthermore, a helical-wheel representation shows that these two cysteine residues are located on opposite sides of the coiled-coil interface (Figure 1E) making it difficult to envision how these two residues could come in close enough proximity to bond. One explanation has been that the two C_{g-1} residues can approach by diffusion and form the disulfide bond, because of the presumed disorder of the DNA-binding regions in the absence of DNA (4,8–10).

FosB/JunD crystal structures in the absence of DNA

To test this theory, we embarked on structural studies of the DNA-free form of FosB/JunD. We first determined that FosB/JunD exists as a disulfide-bonded heterodimer in solution, already upon air-oxidation, after removal of reducing agent (Supplementary Figure S3A–D). We then solved the structure of FosB/JunD under oxidizing and reducing conditions, denoted as FJ^{oxi} and FJ, respectively, in four different crystal forms to a highest resolution of 2.5 Å (FJ^{oxi} type I-III and FJ) (crystallographic data shown in Table 1;

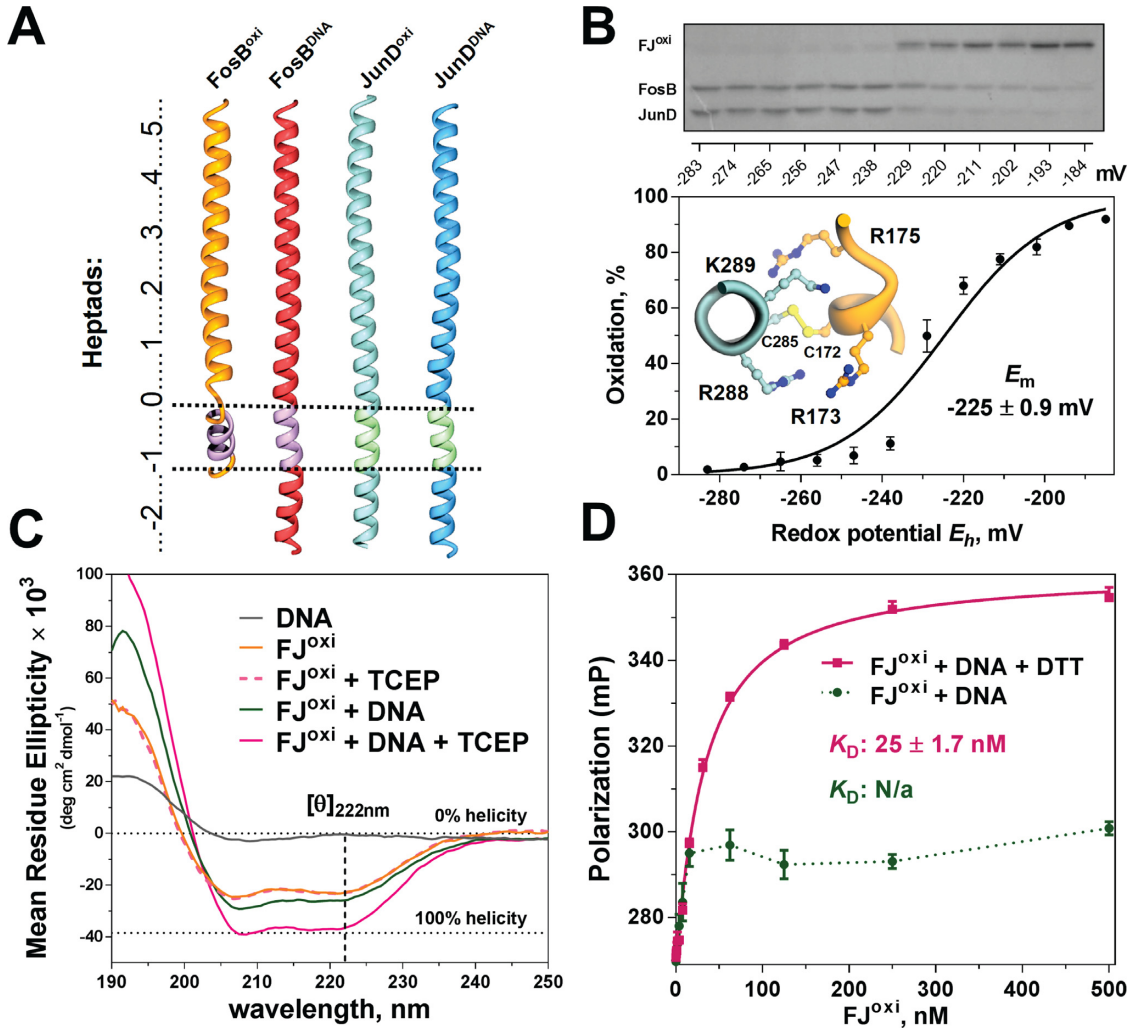

Figure 4. Redox regulation of FosB/JunD *in vitro*. (**A**) Comparison of the FosB and JunD monomers in the FJ^{oxi} and FJ-DNA crystal structures. (**B**) Redox titration of the FosB/JunD bZIP. Error bars represent standard deviations for three replicates. Inset shows the abundance of Arg/Lys residues within 10 Å of the redox-sensitive C^{172} (FosB) and C^{285} (JunD) in FJ^{oxi}. Color scheme is as indicated in Figure 3. (**C**) Circular dichroism spectra of 0.1 mg/ml (6 μM) FJ^{oxi} in the absence and presence of 1 mM TCEP and/or AP-1 DNA at equal molar. Dotted lines indicate 0% and 100% helicity, respectively. (**D**) Titration of FJ^{oxi} heterodimer into 10 nM AP-1 DNA labeled with TAMRA at both 5′-ends in the absence and presence of 1 mM DTT monitored by fluorescence polarization. Error bars indicate the standard deviation for two replicates.

Supplementary Figure S3E–F). As is clear from FJ^{oxi} type I, a close representative for all four crystal structures, the DNA binding motif of both FosB and JunD are unexpectedly ordered even in the absence of DNA (Figure 2A). However, in contrast to JunD where the DNA-binding motif is incorporated as part of a single helix extending the leucine zipper, in FosB, the DNA-binding motif forms an isolated, second helix connected by a kink and is bent by ∼60° (Figure 2A). The shift in the FosB helix registry induced by the kink at R^{175}-R^{176}-R^{177} brings C^{172} (FosB) in close proximity to C^{285} (JunD), allowing an intermolecular disulfide bond to form which covalently tethers a skewed FosB DNA binding motif to the JunD helix (Figure 2B–D). The FJ structure, though solved from crystals grown under reducing conditions, contains both reduced and oxidized C$_{g-1}$ thiol groups located close together in space, and both reveal the kinked conformation of FosB (Figure 2B and C). The kink in FosB is stabilized by K^{289} (K$_{d0}$) of JunD, making a hydrogen bond with the backbone carbonyl groups of R^{175}/R^{176} (R$_{c0}$/R$_{d0}$) of FosB (Figure 2B). The (R/K)$_{d0}$ residues are conserved in all AP-1 and 'AP-1 like' proteins (Figure 1A; Supplementary Figure S1). The FosB/JunD heterodimer in the FJ^{oxi} crystal structures may thus represent a structural template for c-Fos/c-Jun and other bZIPs that contain inter-molecular disulfide bonds formed by C$_{g-1}$ cysteine residues, e.g. CREB (33).

Our findings are striking because the DNA-binding motifs of many bZIP proteins including AP-1 and GCN4 have been presumed to be unfolded, adopting a helical conformation only upon DNA binding (9,11,34). Therefore, in the absence of DNA, while the exemplary bZIP protein GCN4 is thought to be structured only in its leucine zipper (heptad 1–5) (35), our crystal structures suggest that the DNA binding residues of FosB and JunD can adopt a helical conformation in absence of DNA, at least as we observe them in a crystalline environment (Figure 2E).

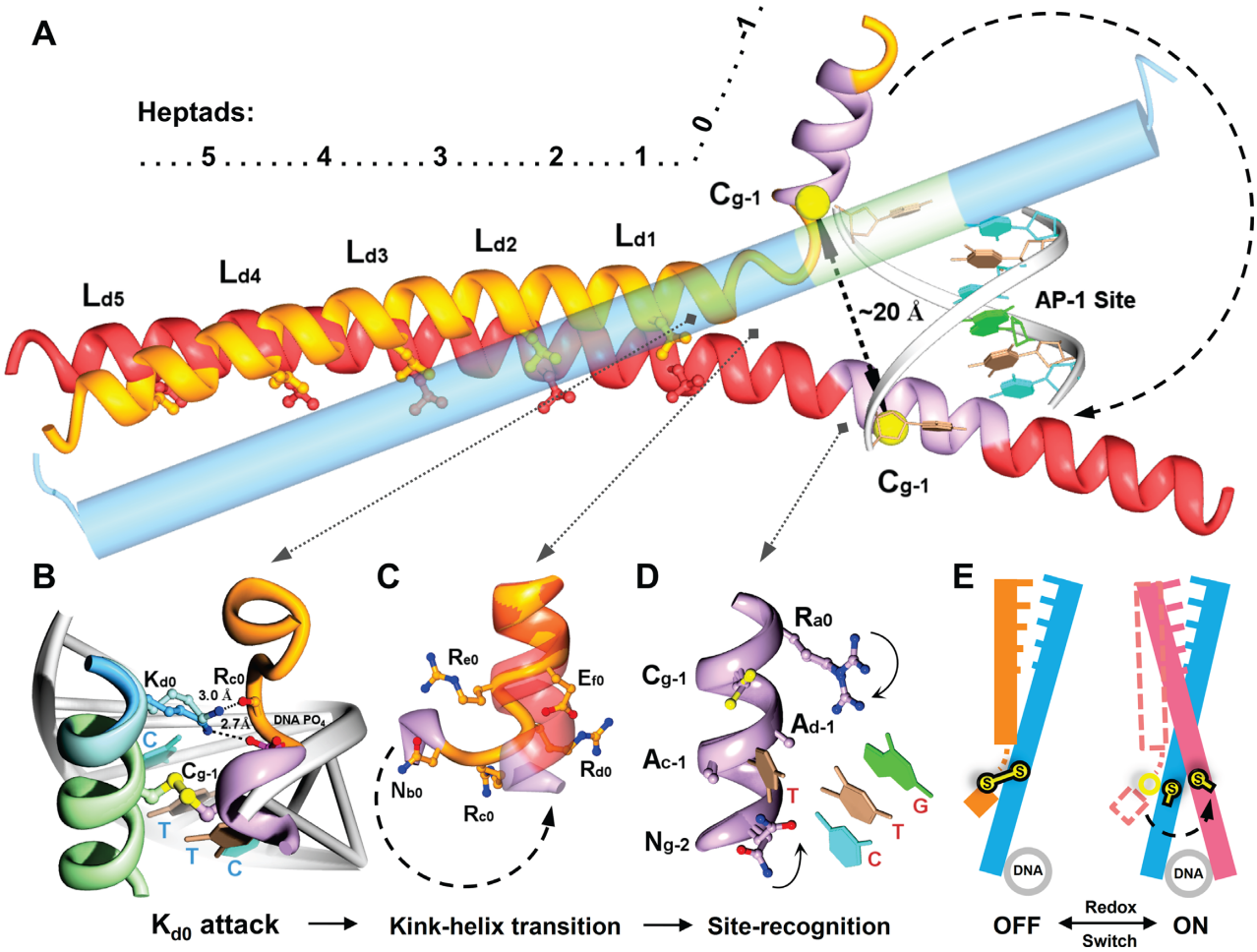

Figure 5. Proposed mechanism of redox-controlled DNA site-recognition by AP-1 Fos/Jun. (**A**) an overview of the FosB (ribbon) structural transition is shown using JunD (tube) as a positional point of reference. The $C_{g\text{-}1}$ residue of FosB (shown as a yellow sphere) undergoes a ∼20 Å movement. FJ^{oxi} type I and FJ-DNA type I were used to construct the illustration. Arrows indicate the conformational rearrangement that FosB must undergo in order to bind DNA. Dashed line represents interatomic distances. (**B**–**D**) K_{d0} attack, kink-helix transition and site-recognition as described in the text. (**E**) Simplified representation shows the redox switch of AP-1 controlling the coupled DNA-binding and structure transition. Color scheme is as indicated in Figure 3. Nucleic acid bases colored as T: brown, G: green, and C: cyan.

Structural transition of FosB upon DNA-binding is controlled by a redox switch

Comparison of our six FosB/JunD structures (±DNA) reveals that the DNA-binding consensus motifs in FosB and JunD retain their helical characters for site recognition regardless of whether DNA is bound (Figures 3 and 4A). However, while the DNA binding motif of JunD is poised to interact with DNA (its position is fixed with respect to the leucine zipper), the DNA binding motif of FosB is swiveled away, anchored by the C^{172}/C^{285} ($C_{g\text{-}1}$) disulfide bond, thus preventing its interaction with the AP-1 site (Figure 3). We propose that the conserved C^{172}/C^{285} ($C_{g\text{-}1}$) intermolecular disulfide bond in FosB/JunD forms a 'redox switch' that controls a structural transition required for DNA binding. Upon reduction (redox switch 'ON'), the FosB bZIP undergoes a localized coil-to-helix transition from an interrupted, kinked helix to a single, continuous helix thereby extending its leucine zipper helix and inserting into the major groove of DNA. When oxidized (redox switch 'OFF'), the $C_{g\text{-}1}$ disulfide bond sterically prevents this structural transition, locking FosB in a kinked conformation that cannot bind DNA (Figure 3).

To measure the sensitivity of the FosB/JunD redox switch to intracellular redox homeostasis, we determined the midpoint redox potential E_m of the FosB/JunD C^{172}/C^{285} ($C_{g\text{-}1}$) disulfide bond at neutral pH revealing it is –225 ± 0.9 mV (Figure 4B; Supplementary Figure S4A-C). The observed redox potential is close to the reported intracellular redox potential (approx. -230 mV) (36) likely rendering the FosB/JunD switch sensitive to perturbation of glutathione as a redox reservoir (36) and redox-active proteins such as redox-factor 1 (Ref-1) and multiprotein bridging factor 1 (MBF1) that modulate AP-1 activity (37–39). The low E_m can be explained by the abundance of positively charged, nucleophilic groups that surround the cysteine residues of the redox switch (R^{288}/R^{175} $(R/K)_{c0}$, K^{289} (K_{d0}) and R^{173} (R_{a0}) sidechains), which could decrease the pK_a of the C^{172}/C^{285} ($C_{g\text{-}1}$) thiol groups (Figure 4B; Supplementary Figure S4D), and are conserved among the aligned sequences (Figure 1A; Supplementary Figure S1).

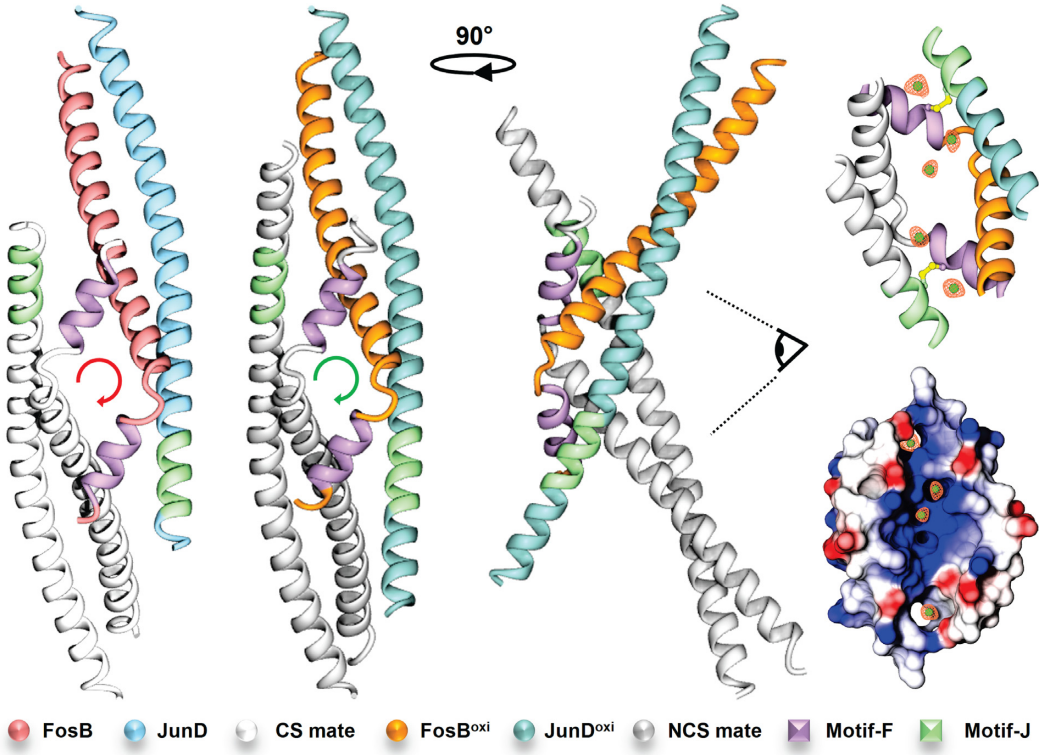

Figure 6. Structural FosB/JunD assembly reveals a binding pocket. A dimer-of-dimers is generated by crystallographic symmetry (CS) or non-crystallographic symmetry (NCS) as exemplified by the FJ and FJ^{oxi} (type I) structures. CS and NCS operations are shown as red and green arrows, respectively. Side view of FJ^{oxi} indicates the location of a pocket; zoomed-in views show the pocket (top right) and its electrostatic surface contour (bottom right). Chloride ions found in the pocket are shown as green spheres and the electron density for these atoms is included ($2mF_o - DF_c$ map contoured at 1.0σ).

In our structures, JunD maintains helicity throughout the bZIP domain, with or without DNA, however, FosB acquires helical content as the kink (heptad 0) and the disordered region beyond the DNA-binding motif (heptad -2 plus the N-terminal residues) rearrange upon DNA binding (Figure 4A). We validated the FosB re-folding event induced by AP-1 DNA with circular dichroism by monitoring the change in ellipticity at 222 nm as an indicator of helical content (Figure 4C; Supplementary Table S1). In the absence of DNA, oxidized and reduced FosB/JunD had the same helical content in solution. Upon addition of DNA to FosB/JunD under reducing conditions the helical content increased significantly, consistent with similar solution studies of c-Fos/c-Jun (9). The apparent increase in helical content (Supplementary Table S1) is likely a combined effect of the refolding of FosB, stabilization of the DNA binding regions of both FosB and JunD, as well as the tighter winding of the leucine zipper in the coiled-coil (see Supplementary Movie S1). However, this DNA-induced increase in helical content was blocked by oxidization of FosB/JunD. We further probed the redox-controlled DNA binding and structure transition of FosB/JunD in fluorescence polarization measurements (Figure 4D). Reduced FosB/JunD efficiently bound a TAMRA-labeled AP-1 site, while the same titration carried out with oxidized FosB/JunD did not (only residual, likely non-specific binding was observed).

Taken together, we propose a generalized mechanism of redox-regulation for AP-1 Fos/Jun transcription factors, which involves a protein structural transition coupled to DNA binding (Figure 5A). When the redox switch is 'OFF' and the C_{g-1} intermolecular disulfide bond is in place, the Jun consensus motif cannot bind to its AP-1 half-site due to steric hindrance of the disulfide-linked Fos. When the redox switch is 'ON', the Jun K_{d0} sidechain interacts with the DNA phosphate backbone, releasing its hydrogen bond to the backbone carbonyl of R_{c0} in the Fos kink ('K_{d0} attack'; Figure 5B). Simultaneously, R_{c0}, R_{d0} and R_{e0} of the Fos kink transition into a helical conformation ('kink-helix transition'; Figure 5C). As the Fos bZIP refolds into a continuous helix, the Fos leucine zipper coils more tightly around the Jun leucine zipper, and the Fos DNA-binding motif pivots to the opposite side of the heterodimer interface and inserts into the major groove of DNA ('site-recognition'; Figure 5D). As a consequence, the C_{g-1} residue of Fos migrates ~20 Å. As long as Fos/Jun remains bound to DNA, the C_{g-1} disulfide bond cannot re-form and the redox switch is kept in the 'ON' state (Figure 5E). The proposed mechanism is consistent with *in vitro* observations that the AP-1 transcription factor c-Fos/c-Jun bZIP domains are incapable of forming a disulfide bond cross-linked heterodimer and bind DNA efficiently when the cysteine residues of the redox switch are mutated to serine, and with studies showing that liberation from redox-regulation leads to increased AP-1 activity (4,8,39–41). Strikingly, JunD pro-

tects cells from oxidants; and seizures (which cause oxidative stress) induce the related ΔFosB (a splice variant of FosB)/JunD (42,43).

Of course, our observations are based on the behavior of the FosB and JunD bZIP domains in a crystalline environment, as well as solution studies involving circular dichroism and fluorescence polarization. It is not clear to what extent the crystalline environment influences the helical propensity of the N-terminal region of the FosB and JunD bZIP domains. Notably however, N-terminal residues Q^{266}-R^{275} of JunD in FJ^{oxi} are helical even though they make no protein-protein interactions or crystal contacts (Supplementary Figure S5). Our work thus raises the possibility that the N-terminal and DNA binding residues of AP-1 bZIP domains can adopt a helical conformation in the absence of DNA. This would set the stage for other proteins, such as co-activators, to bind to the N-terminal regions of bZIP domains to promote the helical conformation of Motif-F and Motif-J (for example through an allosteric mechanism), triggering the formation of 'pre-cast' DNA binding motifs that are fully 'primed' to bind DNA, thereby promoting efficient interaction with DNA.

FosB/JunD assembles as a dimer-of-dimers with a pocket-shaped interface

Our crystal structures suggest a potential binding pocket for small-molecule inhibitors (44). FosB/JunD in the DNA-free form arranged as a dimer-of-dimers in four different crystal environments, i.e. in a head-to-tail arrangement related by 2-fold crystallographic symmetry (crystal form FJ) or by twofold non-crystallographic symmetry (crystal form FJ^{oxi} type I, II, and III) (Figure 6; Supplementary Figure S6). The dimer–dimer interface is predominantly mediated by the two FosB monomers; each FosB DNA binding motif interacts with the opposing FosB leucine zipper helix. The interface generates a concave pocket (~25 × 12 × 6 $Å^3$ in size) which was occupied by chloride ions in several crystal structures (Figure 6; Supplementary Figure S7; Supplementary Movie S2). We confirmed the oligomeric state of FosB/JunD in solution with analytical ultracentrifugation and determined using fluorescence polarization that the equilibrium constant for its formation was in the low micro-molar range, regardless of whether FosB/JunD was oxidized or reduced (Supplementary Figure S8). The oligomeric assembly in all four crystal structures shows relatively flexible basic DNA-binding regions and N-termini of both FosB and JunD, as evidenced by their higher B factors (Supplementary Figure S7B). The oligomeric assembly likely helped stabilize the kink in FosB and DNA-binding motifs of FosB and JunD enabling us to observe these relatively flexible regions in our crystal structures.

Together, the structural and mechanistic insights into FosB/JunD suggest directions for therapeutically targeting AP-1 transcription factors focused on designing small molecules that alter the redox switch of AP-1 or stabilize the oligomer interface disrupting its binding to DNA (44–46).

ACCESSION NUMBERS

Atomic coordinates and structure factors for the FJ-DNA (type I), FJ-DNA (type II), FJ, FJ^{oxi} (type I), FJ^{oxi} (type II) and FJ^{oxi} (type III) crystal structures are deposited in the Protein Data Bank under accession codes 5VPE, 5VPF, 5VPA, 5VPB, 5VPC and 5VPD, respectively.

SUPPLEMENTARY DATA

Supplementary Data are available at NAR Online.

ACKNOWLEDGEMENTS

We thank the staff at the Advanced Photon Source Beamline 17-ID, 19-ID and 21-ID for assistance during data collection. DNA-sequencing and protein mass-spectrometry services were provided by the Next Generation Sequencing Core Facility and the Mass Spectrometry Core at UTMB. G.R. and E.J.N. supervised the project. Z.Y. designed and performed all experiments except DNA-sequencing and mass spectrometry, analyzed all data and drafted the manuscript. M.M. analyzed and commented on the crystal structures. All authors contributed to the manuscript. Drs. M. White and L. Holthauzen (SCSB) are thanked for helpful discussions.

FUNDING

National Institutes of Health [R01 DA040621]; Brain and Behavior Research Foundation; Sealy Center for Structural and Molecular Biology (SCSB) at the University of Texas Medical Branch (UTMB). Funding for open access charge: National Institutes of Health.
Conflict of interest statement. None declared.

REFERENCES

1. Shlomai,J. (2010) Redox control of protein-DNA interactions: from molecular mechanisms to significance in signal transduction, gene expression, and DNA replication. *Antioxid. Redox Signal.*, **13**, 1429–1476.
2. Liu,H., Colavitti,R., Rovira,II and Finkel,T. (2005) Redox-dependent transcriptional regulation. *Circ. Res.*, **97**, 967–974.
3. Amoutzias,G.D., Bornberg-Bauer,E., Oliver,S.G. and Robertson,D.L. (2006) Reduction/oxidation-phosphorylation control of DNA binding in the bZIP dimerization network. *BMC Genomics*, **7**, 107.
4. Abate,C., Patel,L., Rauscher,F.J. 3rd and Curran,T. (1990) Redox regulation of fos and jun DNA-binding activity in vitro. *Science*, **249**, 1157–1161.
5. Shaulian,E. and Karin,M. (2002) AP-1 as a regulator of cell life and death. *Nat Cell Biol*, **4**, E131–E136.
6. Glover,J.N. and Harrison,S.C. (1995) Crystal structure of the heterodimeric bZIP transcription factor c-Fos-c-Jun bound to DNA. *Nature*, **373**, 257–261.
7. Gentz,R., Rauscher,F.J. 3rd, Abate,C. and Curran,T. (1989) Parallel association of Fos and Jun leucine zippers juxtaposes DNA binding domains. *Science*, **243**, 1695–1699.
8. Bannister,A.J., Cook,A. and Kouzarides,T. (1991) In vitro DNA binding activity of Fos/Jun and BZLF1 but not C/EBP is affected by redox changes. *Oncogene*, **6**, 1243–1250.
9. Patel,L., Abate,C. and Curran,T. (1990) Altered protein conformation on DNA binding by Fos and Jun. *Nature*, **347**, 572–575.
10. Seldeen,K.L., McDonald,C.B., Deegan,B.J. and Farooq,A. (2008) Coupling of folding and DNA-binding in the bZIP domains of Jun-Fos heterodimeric transcription factor. *Arch. Biochem. Biophys.*, **473**, 48–60.

11. Das,R.K., Crick,S.L. and Pappu,R.V. (2012) N-terminal segments modulate the alpha-helical propensities of the intrinsically disordered basic regions of bZIP proteins. *J. Mol. Biol.*, **416**, 287–299.
12. Nestler,E.J. (2008) Review. Transcriptional mechanisms of addiction: role of DeltaFosB. *Philos. Trans. R. Soc. Lond. B. Biol. Sci.*, **363**, 3245–3255.
13. Otwinowski,Z. and Minor,W. (1997) [20] Processing of X-ray diffraction data collected in oscillation mode. *Methods Enzymol.*, **276**, 307–326.
14. McCoy,A.J., Grosse-Kunstleve,R.W., Adams,P.D., Winn,M.D., Storoni,L.C. and Read,R.J. (2007) Phaser crystallographic software. *J. Appl. Crystallogr.*, **40**, 658–674.
15. Adams,P.D., Afonine,P.V., Bunkoczi,G., Chen,V.B., Davis,I.W., Echols,N., Headd,J.J., Hung,L.W., Kapral,G.J., Grosse-Kunstleve,R.W. *et al.* (2010) PHENIX: a comprehensive Python-based system for macromolecular structure solution. *Acta Crystallogr. D, Biol. Crystallogr.*, **66**, 213–221.
16. Emsley,P. and Cowtan,K. (2004) Coot: model-building tools for molecular graphics. *Acta Crystallogr. D, Biol. Crystallogr.*, **60**, 2126–2132.
17. Adams,P.D., Grosse-Kunstleve,R.W., Hung,L.W., Ioerger,T.R., McCoy,A.J., Moriarty,N.W., Read,R.J., Sacchettini,J.C., Sauter,N.K. and Terwilliger,T.C. (2002) PHENIX: building new software for automated crystallographic structure determination. *Acta Crystallogr. D, Biol. Crystallogr.*, **58**, 1948–1954.
18. Painter,J. and Merritt,E.A. (2006) Optimal description of a protein structure in terms of multiple groups undergoing TLS motion. *Acta Crystallogr. D, Biol. Crystallogr.*, **62**, 439–450.
19. Chen,V.B., Arendall,W.B. 3rd, Headd,J.J., Keedy,D.A., Immormino,R.M., Kapral,G.J., Murray,L.W., Richardson,J.S. and Richardson,D.C. (2010) MolProbity: all-atom structure validation for macromolecular crystallography. *Acta Crystallogr. D, Biol. Crystallogr.*, **66**, 12–21.
20. McNicholas,S., Potterton,E., Wilson,K.S. and Noble,M.E. (2011) Presenting your structures: the CCP4mg molecular-graphics software. *Acta Crystallogr. D, Biol. Crystallogr.*, **67**, 386–394.
21. Pettersen,E.F., Goddard,T.D., Huang,C.C., Couch,G.S., Greenblatt,D.M., Meng,E.C. and Ferrin,T.E. (2004) UCSF Chimera–a visualization system for exploratory research and analysis. *J. Comput. Chem.*, **25**, 1605–1612.
22. Papadopoulos,J.S. and Agarwala,R. (2007) COBALT: constraint-based alignment tool for multiple protein sequences. *Bioinformatics*, **23**, 1073–1079.
23. Cox,A.G., Peskin,A.V., Paton,L.N., Winterbourn,C.C. and Hampton,M.B. (2009) Redox potential and peroxide reactivity of human peroxiredoxin 3. *Biochemistry*, **48**, 6495–6501.
24. Hutchison,R.S. and Ort,D.R. (1995) Measurement of equilibrium midpoint potentials of thiol/disulfide regulatory groups on thioredoxin-activated chloroplast enzymes. *Methods Enzymol*., **252**, 220–228.
25. Scholtz,J.M., Qian,H., York,E.J., Stewart,J.M. and Baldwin,R.L. (1991) Parameters of helix-coil transition theory for alanine-based peptides of varying chain lengths in water. *Biopolymers*, **31**, 1463–1470.
26. Veldkamp,C.T., Peterson,F.C., Pelzek,A.J. and Volkman,B.F. (2005) The monomer-dimer equilibrium of stromal cell-derived factor-1 (CXCL 12) is altered by pH, phosphate, sulfate, and heparin. *Protein Sci.*, **14**, 1071–1081.
27. Hulme,E.C. and Trevethick,M.A. (2010) Ligand binding assays at equilibrium: validation and interpretation. *Br. J. Pharmacol.*, **161**, 1219–1237.
28. Laue,T.M., Shah,B.D., Ridgeway,T.M. and Pelletier,S.L. (1992) In: Harding,S and Rowe,A (eds). *Analyticall Ultracentrifugation in Biochemistry and Polymer Science*. Royal Society of Chemistry, pp. 90–125.
29. Schuck,P. (2000) Size-distribution analysis of macromolecules by sedimentation velocity ultracentrifugation and lamm equation modeling. *Biophys. J.*, **78**, 1606–1619.
30. Schuck,P. (2003) On the analysis of protein self-association by sedimentation velocity analytical ultracentrifugation. *Anal. Biochem.*, **320**, 104–124.
31. Brown,P.H. and Schuck,P. (2006) Macromolecular size-and-shape distributions by sedimentation velocity analytical ultracentrifugation. *Biophys. J.*, **90**, 4651–4661.
32. Leonard,D.A., Rajaram,N. and Kerppola,T.K. (1997) Structural basis of DNA bending and oriented heterodimer binding by the basic leucine zipper domains of Fos and Jun. *Proc. Natl. Acad. Sci. U.S.A.*, **94**, 4913–4918.
33. Goren,I., Tavor,E., Goldblum,A. and Honigman,A. (2001) Two cysteine residues in the DNA-binding domain of CREB control binding to CRE and CREB-mediated gene expression. *J. Mol. Biol.*, **313**, 695–709.
34. Weiss,M.A., Ellenberger,T., Wobbe,C.R., Lee,J.P., Harrison,S.C. and Struhl,K. (1990) Folding transition in the DNA-binding domain of GCN4 on specific binding to DNA. *Nature*, **347**, 575–578.
35. O'Shea,E.K., Klemm,J.D., Kim,P.S. and Alber,T. (1991) X-ray structure of the GCN4 leucine zipper, a two-stranded, parallel coiled coil. *Science*, **254**, 539–544.
36. Hwang,C., Sinskey,A.J. and Lodish,H.F. (1992) Oxidized redox state of glutathione in the endoplasmic reticulum. *Science*, **257**, 1496–1502.
37. Xanthoudakis,S. and Curran,T. (1992) Identification and characterization of Ref-1, a nuclear protein that facilitates AP-1 DNA-binding activity. *EMBO J.*, **11**, 653–665.
38. Xanthoudakis,S., Miao,G., Wang,F., Pan,Y.C. and Curran,T. (1992) Redox activation of Fos-Jun DNA binding activity is mediated by a DNA repair enzyme. *EMBO J.*, **11**, 3323–3335.
39. Jindra,M., Gaziova,I., Uhlirova,M., Okabe,M., Hiromi,Y. and Hirose,S. (2004) Coactivator MBF1 preserves the redox-dependent AP-1 activity during oxidative stress in Drosophila. *EMBO J.*, **23**, 3538–3547.
40. Ng,L., Forrest,D. and Curran,T. (1993) Differential roles for Fos and Jun in DNA-binding: redox-dependent and independent functions. *Nucleic Acids Res.*, **21**, 5831–5837.
41. Okuno,H., Akahori,A., Sato,H., Xanthoudakis,S., Curran,T. and Iba,H. (1993) Escape from redox regulation enhances the transforming activity of Fos. *Oncogene*, **8**, 695–701.
42. Gerald,D., Berra,E., Frapart,Y.M., Chan,D.A., Giaccia,A.J., Mansuy,D., Pouyssegur,J., Yaniv,M. and Mechta-Grigoriou,F. (2004) JunD reduces tumor angiogenesis by protecting cells from oxidative stress. *Cell*, **118**, 781–794.
43. Chen,J., Nye,H.E., Kelz,M.B., Hiroi,N., Nakabeppu,Y., Hope,B.T. and Nestler,E.J. (1995) Regulation of delta FosB and FosB-like proteins by electroconvulsive seizure and cocaine treatments. *Mol. Pharmacol.*, **48**, 880–889.
44. Ye,N., Ding,Y., Wild,C., Shen,Q. and Zhou,J. (2014) Small molecule inhibitors targeting activator protein 1 (AP-1). *J. Med. Chem.*, **57**, 6930–6948.
45. Aikawa,Y., Morimoto,K., Yamamoto,T., Chaki,H., Hashiramoto,A., Narita,H., Hirono,S. and Shiozawa,S. (2008) Treatment of arthritis with a selective inhibitor of c-Fos/activator protein-1. *Nat. Biotechnol.*, **26**, 817–823.
46. Wang,Y., Cesena,T.I., Ohnishi,Y., Burger-Caplan,R., Lam,V., Kirchhoff,P.D., Larsen,S.D., Larsen,M.J., Nestler,E.J. and Rudenko,G. (2012) Small molecule screening identifies regulators of the transcription factor DeltaFosB. *ACS Chem. Neurosci.*, **3**, 546–556.